RSC Advances

PAPER

View Article Online
View Journal | View Issue



Cite this: *RSC Adv.*, 2020, **10**, 23263

# Synergistic effects of dopant (Ti or Sn) and oxygen vacancy on the electronic properties of hematite: a DFT investigation†

Haijun Pan, *[ab] Dongbiao Ao[a] and Gaowu Qin[c]

Hematite has been widely studied as one of the most promising photoanodes in the photoelectrochemical decomposition of water. At present, a prevailing strategy of coupling dopant (Ti or Sn) with oxygen vacancies has been proposed by experiment, and effectively improves the photocatalytic activity. In order to clarify the intrinsic reasons for the improvement of the photochemical activity, density functional theory is adopted to calculate the formation mechanism and electronic properties of hematite with doping ions and oxygen vacancies. The result shows that the doped atom is beneficial to the formation of oxygen vacancies in hematite, thus forming a stable structure containing doping ions and oxygen vacancies. Due to the synergistic effects of dopant and oxygen vacancies, the bandgap of hematite decreases, and donor levels are introduced into the bandgap, which lead to the increase of carrier concentration. In the system with doped Ti and oxygen vacancies, donor levels are introduced at 1.47 eV and 1.73 eV below the bottom of the conduction band, respectively. For the case containing Sn and oxygen vacancies, the donor level is introduced at 1.75 eV from the conduction band minimum. Our results elaborate the reasons for the enhancement of carrier densities in terms of electronic structure, and provide some guidance for the future modification of photocatalysts.

Received 15th February 2020
Accepted 3rd June 2020

DOI: 10.1039/d0ra01450h

rsc.li/rsc-advances



## Introduction

Since Fujishima used $TiO_2$ to split water into $H_2$ under ultraviolet light, photoelectrochemical (PEC) systems have long been considered as methods to produce clean hydrogen by solar energy harvesting, gradually becoming the focus of world attention.[1] Among various oxide semiconductor photocatalysts, hematite ($\alpha$-$Fe_2O_3$) has been capturing considerable research attention by serving as a water oxidation photoanode. Hematite is abundant in minerals, non-toxic and chemically stable in aqueous solution. In addition, hematite has a favorable bandgap (~2.2 eV), which corresponds to the major part of the solar spectrum.[2,3] What is more, its valence band locates below the oxidation potential of water, possessing strong oxidation ability.[4] Theoretically, the solar to hydrogen (STH) efficiency of $Fe_2O_3$ can reach as high as 12.9%, with a photocurrent density of 12.6 mA $cm^{-2}$.[5] However, the reported efficiency of hematite is much less than the theoretical value. Generally, the reason for this inconsistency lies in the short hole-diffusion length (2–4 nm),[6] the short lifetimes of the excited electrons (<10 ps),[7] and low electron mobility in hematite.[8]

Doping has been employed as one of the important methods in improving the photocatalytic performance of $Fe_2O_3$. Among numerous doped ions, $Sn^{4+}$ doping[9–13] and $Ti^{4+}$ doping[14–17] can greatly enhance the photocatalytic activity and photocurrent of $Fe_2O_3$. The experimental and theoretical analysis show that enhancement of its photocatalytic activity is mainly due to the increase of carrier concentration, the reduction of electron–hole recombination rate and the decrease of optical bandgap. Also, doping can alert the interfacial properties between catalyst and electrolyte, such as electric field across the space charge layer and charge transfer kinetics.

Preparation of oxygen vacancy ($V_O$) in $Fe_2O_3$ has been proved to be another effective method to improve its photocatalytic activity. Experimentally, Ling *et al.* decomposed the β-FeOOH nanowires at 550 °C in an oxygen-deficient condition to obtain hematite nanowires containing oxygen vacancies, which yielded a substantially enhanced photocurrent density.[18] Li *et al.* present the preparation of $H_2$-treated hematite nanostructures by a pyrolysis of $NaBH_4$ in a crucible.[19] The $H_2$-treated hematite photoelectrode displays a photocurrent of 2.28 mA $cm^{-2}$ at 1.23 V *vs.* RHE, which is over 2.5 times higher than that of pristine hematite. Rioult *et al.* prepare the single crystalline film of hematite through atomic oxygen assisted molecular beam epitaxy, and adjust the concentration of oxygen vacancy through

[a]School of Resources and Materials, Northeastern University at Qinhuangdao, Qinhuangdao 066004, People's Republic of China. E-mail: panhaijun@neuq.edu.cn
[b]Key Laboratory of Dielectric and Electrolyte Functional Materials Hebei Province, Qinhuangdao 066004, People's Republic of China
[c]Key Laboratory for Anisotropy and Texture of Materials, Northeastern University, Shenyang 110819, People's Republic of China

† Electronic supplementary information (ESI) available. See DOI: 10.1039/d0ra01450h

annealing in UHV.[20] For the optimal oxygen vacancy concentration, the sample shows a 50% photocurrent gain and reduction for the onset potential by 0.2 V with respect to stoichiometric hematite. In terms of electronic properties, the formation of oxygen vacancies is supposed to lead to an increase in donor concentration in $Fe_2O_3$.

From a design perspective, synergistic effect of ion doping and oxygen vacancy can produce a cumulative effect on electronic properties, which is necessary to achieve sufficiently higher photocatalytic efficiency. Experimentally, many researchers have found that the presence of oxygen vacancy can further enhance the photocatalytic performance of doped $Fe_2O_3$. Through control of the oxygen partial pressure, Sn doped hematite with $V_O$ can exhibit a higher photocurrent than that of normally prepared hematite. This enhancement can be attributed to the improvement of electrical conductivity due to carrier generation from defects.[21] The results obtained by Pu *et al.* suggest that oxygen vacancies in Ti doped hematite mainly affect the performance by improving the donor densities with lower oxidation state of Fe, while Ti-doping might affect the performance of hematite by surface catalytic effects or more active sites for water oxidation.[22] Wang *et al.* conclude that the presence of $V_O$ can not only promote surface electrocatalytic oxygen evolution reaction (OER) processes, but also increase the carrier concentration.[23] Zhou *et al.* annealed Sn doped $Fe_2O_3$ in a reducing atmosphere created by partial oxidation of graphite to produce oxygen vacancies. The donor density increases by 73% in Sn-doped $Fe_2O_3$ annealed on graphite at 770 °C for 20 min, and ~70% enhancement in photocurrent density is observed.[24] Other experiments also indicate that carrier densities or conductivity enhancement is one of key reasons for the enhanced photoactivity.[25,26] Actually, the existence of oxygen vacancies and doped ions in $Fe_2O_3$ is very complex, and synergistic effects of them on the electronic properties of hematite are still not clear.

This paper mainly focus on the interaction between oxygen vacancy and doped ion in $Fe_2O_3$, and the corresponding electronic properties in order to reveal the fundamental reasons for the improvement of photocatalytic performance. The results indicate that the doped atom (Sn or Ti) is beneficial to the formation of oxygen vacancy in hematite. In addition to reducing the bandgap width, the synergistic effects of oxygen vacancy and doping can introduce donor levels into the bandgap, which is responsible for improvement of electrical conductivity.

## Computational methods

Hematite has a hexagonal close-packed crystal structure with the space group of $R\bar{3}2/C$ (no. 167), and one unit cell contains 12 Fe and 18 O atoms. Here, we construct a 120-atom 2 × 2 × 1 supercell in order to understand synergistic effects of doping and oxygen vacancy on the electronic properties of hematite, which are shown in Fig. 1(a). For metal atom doping, we use one metal atom (Ti or Sn) to replace one Fe atom in the supercell. As for oxygen vacancy, one of equivalent O atoms is artificially removed. As can be seen in Fig. 1(b), the supercell containing

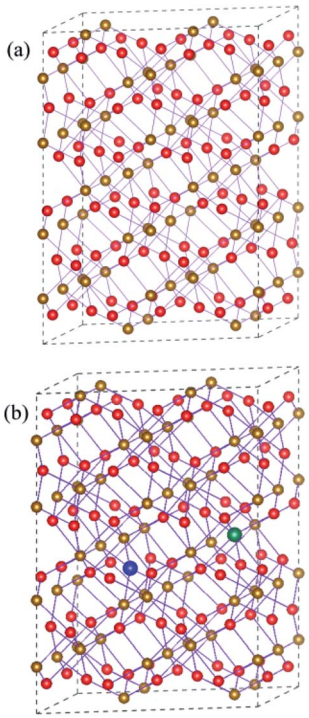


Fig. 1 (a) Schematic plot of the 2 × 2 × 1 supercell of $Fe_2O_3$ (b) the supercell of $Fe_2O_3$ containing $V_O$ and dopant. The Fe atom and O atom are represented by golden yellow and red spheres, respectively. $V_O$ and dopant are represented by blue and green spheres, respectively.

doped atom and oxygen vacancy is modelled by replacing a Fe atom with a metal atom around the oxygen vacancy. In addition to the most stable model mentioned above, other possible models have been carefully examined, which are provided in Fig. S1 and Table S1 in the ESI.†

All calculations are performed in the framework of the spin-polarized density functional theory with Vienna *ab initio* simulation package (VASP) code.[27] The valence electron and ion core interactions are described by the projector augmented wave (PAW) potential.[28] The exchange–correlation potential is described by generalized gradient approximation (GGA) with the Perdew–Burke–Ernzerhof (PBE) scheme.[29] The cutoff energy for electronic wave functions is 500 eV, which is high enough for energy convergence. The Brillouin-zone integration is performed using Monkhorst–Pack grids of 3 × 3 × 1.[30] The lattice parameters and atomic positions of pure and doped hematite are fully relaxed using a conjugate gradient minimization algorithm until force convergence of 1 meV $Å^{-1}$ and energy convergence of $10^{-5}$ eV are reached. The framework of GGA + U invented by Dudarev *et al.* is selected in this simulation.[31] The value of U–J is set to 4.3 eV, which is symmetrically picked out by Mosey *et al.*[32]

## Results and discussion

### The formation energy

The formation energies of various defects in $Fe_2O_3$ are investigated in order to know the growth mechanism and relative

 

stability of new systems. With respect to neutral defects in $Fe_2O_3$, the formation energies can be calculated as follows:[33]

$$E(V_O)_f = E(V_O) - E(\text{pure}) + \mu_O$$

$$E(M_{Fe})_f = E(M_{Fe}) - E(\text{pure}) - \mu_M + \mu_{Fe}$$

$$E(M_{Fe} + V_O)_f = E(M_{Fe} + V_O) - E(\text{pure}) - \mu_M + \mu_{Fe} + \mu_O$$

$E$(pure) is the total energy of the hematite 2 × 2 × 1 supercell. $E(V_O)$, $E(M_{Fe})$ and $E(M_{Fe} + V_O)$ are the total energy of the systems containing $V_O$, $M_{Fe} = Ti_{Fe}$ or $Sn_{Fe}$, and $(M_{Fe} + V_O)$, respectively. $\mu_M$, $\mu_{Fe}$ and $\mu_O$ represent the chemical potential of M, Fe, and O, respectively.

As is well known, the chemical potential is closely related to the sample growth condition, which could be very different from O-rich to Fe-rich conditions. Under Fe-rich growth condition, the chemical potential $\mu_{Fe}$ is calculated from the energy of one bulk Fe atom, and the corresponding $\mu_O$ can be obtained from $\mu_{Fe_2O_3} = 2\mu_{Fe} + 3\mu_O$. Under O-rich condition, the chemical potential $\mu_O$ is determined by half of the energy of an $O_2$ molecule, and the $\mu_{Fe}$ can be calculated from the formula above. The formation energy as a function of oxygen chemical potential is plotted in Fig. 2. Regardless of the preparation conditions, the formation energy of oxygen vacancy is always positive, indicating that the formation of oxygen vacancy will be inhibited during the growth of $Fe_2O_3$. Relatively small formation energy of $Ti_{Fe}$ ($Sn_{Fe}$) over the entire range of $\mu_O$ illustrates that Ti (Sn) substitution for Fe can be easily achieved, which has been confirmed by experimental results. More interestingly, the formation energy of $Ti_{Fe}$ (or $Sn_{Fe}$) and oxygen vacancy is much lower than that of oxygen vacancy in $Fe_2O_3$. This result shows that the introduction of doped ions would promote the occurrence of oxygen vacancy. In experiment, Pu *et al.* verifies the production of oxygen vacancy in Ti-doped hematite could be easier compared to that in undoped hematite under a moderate partial oxygen pressure range.[22]

## Electronic structures

In this section, we first analyze the electronic structure and charge distribution of $Fe_2O_3$ with low concentration dopant.

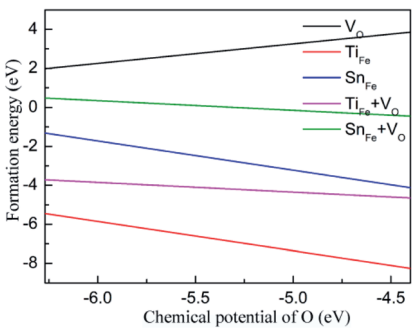


Fig. 2 The formation energy of $V_O$, $Ti_{Fe}$, $Sn_{Fe}$, $Ti_{Fe} + V_O$ or $Sn_{Fe} + V_O$ as a function of the chemical potential of O.

Furthermore, we discuss the changes of them caused by the interaction between oxygen vacancy and doped ions, so as to explain the nature of the enhancement of photocatalytic properties observed in experiments.

In Fig. 3(a1), it can be found that the Fe 3d states are the main component of conduction band minimum, and the valence band maximum is composed of Fe 3d and O 2p states. It is reported that the hematite possess a stable antiferromagnetic (AFM) ground state below −10 °C, in which the magnetic moment direction of Fe atom is along the [0001]. In Fig. 3(a2) and (a3), density of states of a single atom is plotted. It shows that Fe 3d electrons have weak interaction with O 2p electrons in the range of −8–−4 eV, which leads to the emergence of unpaired spin electrons. Thus, the magnetic moment on the Fe atom mainly originates from these unpaired Fe 3d electrons in this energy range. The calculated magnetic moment around iron atoms is 4.15 $\mu_B$, which is consistent with the experimental results in the literature.[34,35] The bandgap is predicted to be 2.20 eV. The electronic structure of pristine $Fe_2O_3$ is consistent with previous computational observations.[14] For charge transfer in $Fe_2O_3$, Bader charge analysis (Fig. S2a†) points out that the Fe atom loses 1.72e to surrounding O atoms, and O atom obtains 1.15e from nearby Fe atoms. Correspondingly, the XPS result in the experiment indicates that the Fe and O atom convert to $Fe^{3+}$ and $O^{2-}$ state after the formation of $Fe_2O_3$, respectively.[36]

The introduction of oxygen vacancy changes local atomic structure and the interaction between O and Fe atoms, leading to a significant change in the electronic structure of $Fe_2O_3$. Fig. 3(b2) and (b3) shows the electronic density of states of typical O and Fe atoms near the oxygen vacancy. Compared with pristine $Fe_2O_3$, it can be seen that there is a stronger interaction between the Fe 3d orbital electrons and the surrounding O 2p electrons in −6–0 eV. Therefore, the number of spin unpaired electrons in Fe 3d orbital decreases, and magnetic moment of Fe atom reduces to 3.69 $\mu_B$. Due to the presence of oxygen vacancy, only 1.33 charges are supplied to the lattice by the surrounding iron atoms.

For Ti doping at low concentration, electronic structure (Fig. 4(a4)) shows that hybrid orbits are first formed by 3d and 4s orbitals of Ti atom, and then interact with O 2p orbitals. In Fig. S3c,† the Bader charge analysis indicates that the doped Ti atom will lose 1.94e to the $Fe_2O_3$ lattice. Although Ti atom has one more valence electron than Fe atom, the charge on oxygen atoms surrounding Ti atom does not increase compared to undoped $Fe_2O_3$. The reason for this phenomenon is that the introduction of Ti atoms weakens the interaction between the surrounding O atoms and Fe atoms, which reduces the charge transfer between Fe and O atoms. At the same time, the charge on the Fe atoms will increase. The electronic property of the Fe atom closest to the Ti atom in the adjacent atomic layer is the most sensitive to this lattice distortion. Fig. 4(a2) and (a3) state that Fe 3d electrons have a strong hybridization with O 2p electrons in the range of −6–0 eV. On this typical Fe atom, the magnetic moment is changed into 3.60 $\mu_B$.

For Sn doping at low concentration, electronic structure (Fig. 4(b4)) shows that hybrid orbits are first formed by 5s and 5p orbitals of Sn atom, and then interact with O 2p orbitals. In

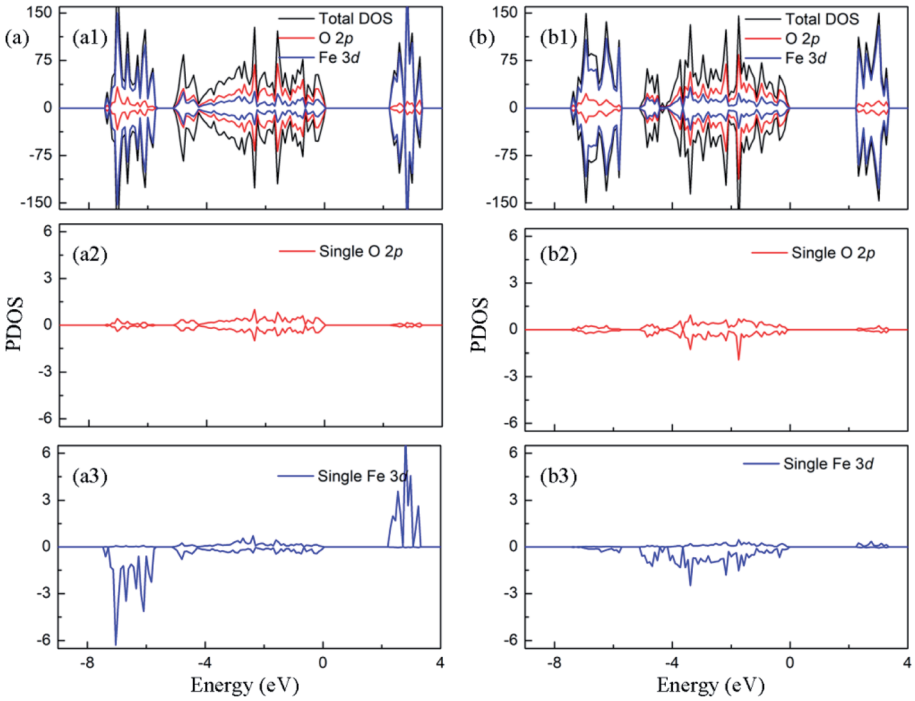


Fig. 3 The projected density of states of (a) perfect $Fe_2O_3$ and (b) $Fe_2O_3$ containing $V_O$. The Fermi level is set to zero.

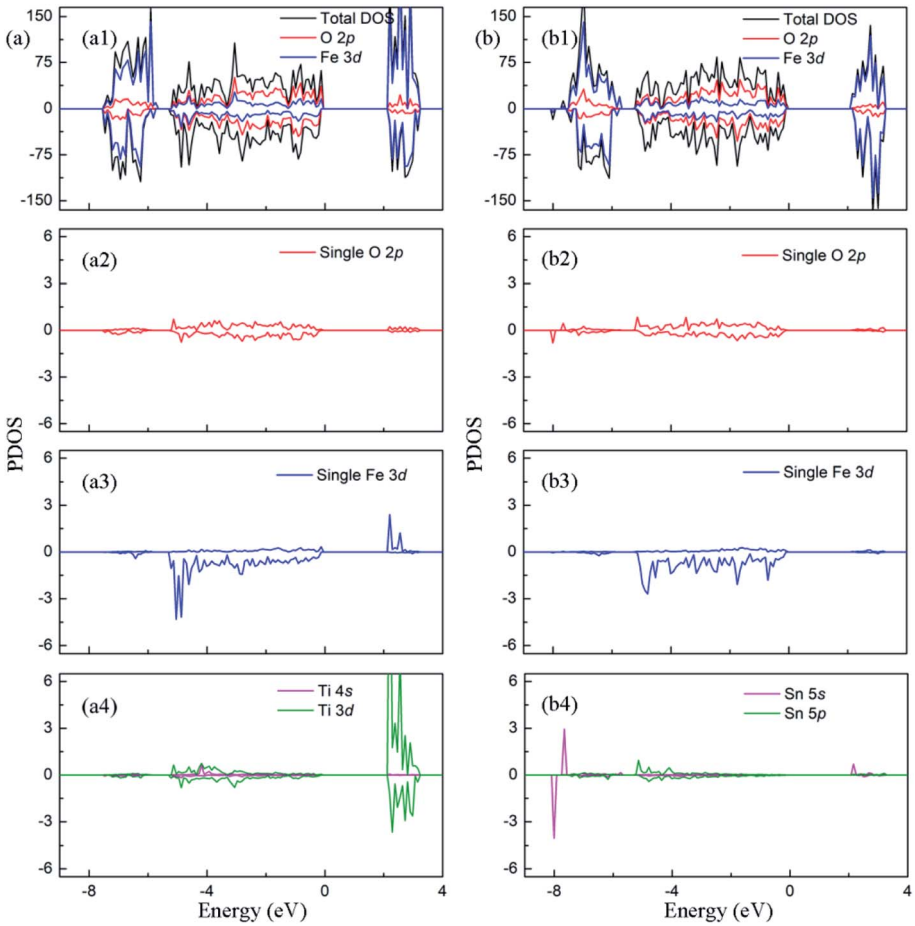


Fig. 4 The projected density of states of (a)Ti doped $Fe_2O_3$ and (b) Sn doped $Fe_2O_3$. The Fermi level is set to zero.

 

this process, Sn atom will provide 2.28e to the crystal lattice, displaying a stronger degree of ionization than Fe atom, while the surrounding oxygen atoms get 1.17e. The experimental results show that Sn atom possesses 4+ state in Sn doped $Fe_2O_3$. Compared to pure hematite, an extra electron would be introduced by $Sn^{4+}$ and hope between $Fe^{3+}$ ions. The calculation result shows that the extra electron mainly distributes over oxygen atoms, and needs to be excited from O 2p to Fe 3d before transfer across the $Fe^{3+}$ ions.[9] As with Ti doping, Sn doping can also change the bonding mode between Fe and O atoms(shown in Fig. 4(b)). The magnetic moment on the typical Fe atom becomes to 3.62 $\mu_B$.

In order to clarify the enhancement of photocatalytic activity observed by experiments, the change of electronic properties caused by the presence of doped ion and oxygen vacancy are calculated. The density of states of $(Ti_{Fe} + V_O)$–$Fe_2O_3$ is plotted in Fig. 5(a). The spin-up and -down donor states are introduced at 1.47 eV and 1.73 eV from the bottom of the conduction band minimum, respectively. As shown in Fig. 5(a2) and (a3), the interaction between Fe 3d and O 2p electrons in the range of −1–−6 eV reduces the number of unpaired electrons in 3d orbit, which leads to the reduction of the magnetic moment on Fe atom (3.60 $\mu_B$). Besides, it also contributes to the local donor levels, which indicates the emergence of $Fe^{2+}$ ion.[37] In order to explain the formation of donor levels, the average changes of Fe–O bond length around oxygen vacancy are compared when various defects appear. In $Fe_2O_3$ containing O vacancy, the bond length of the Fe–O bond around the oxygen vacancy decreases by about 0.026 Å on average, indicating that the five coordinated Fe atom has stronger interaction with the surrounding O atom. Thus, there are no mid-gap levels in Fig. 3(b). In $(Ti_{Fe} + V_O)$–$Fe_2O_3$, the average increase of Fe–O bond length is about 0.008 Å for the five coordinated Fe atom. By comparing the change of bond length, it is pointed out that the additional nonlocal electrons brought by Ti will weaken the bonding strength between the Fe and O atoms near the O vacancy, which cause the increase of the unbonded electrons in Fe atoms. Therefore, the properties of the donor states mainly possess the electronic properties of Fe 3d and O 2p. The Bader charge analysis shows that there are 6.68e on each Fe atom adjacent to O vacancy, which is 0.5e more than that in the perfect $Fe_2O_3$. The partial charge density of the intermediate state is plotted in Fig. S3.† It points out that the partial charge density of donor states is mainly distributed on the Fe atom around the O vacancy than others. In addition, the bandgap width decreased to 2.07 eV due to the downward movement of the conduction band. The density of states of $(Sn_{Fe} + V_O)$–$Fe_2O_3$ is plotted in Fig. 5(b). The donor level is introduced at 1.75 eV from the conduction band

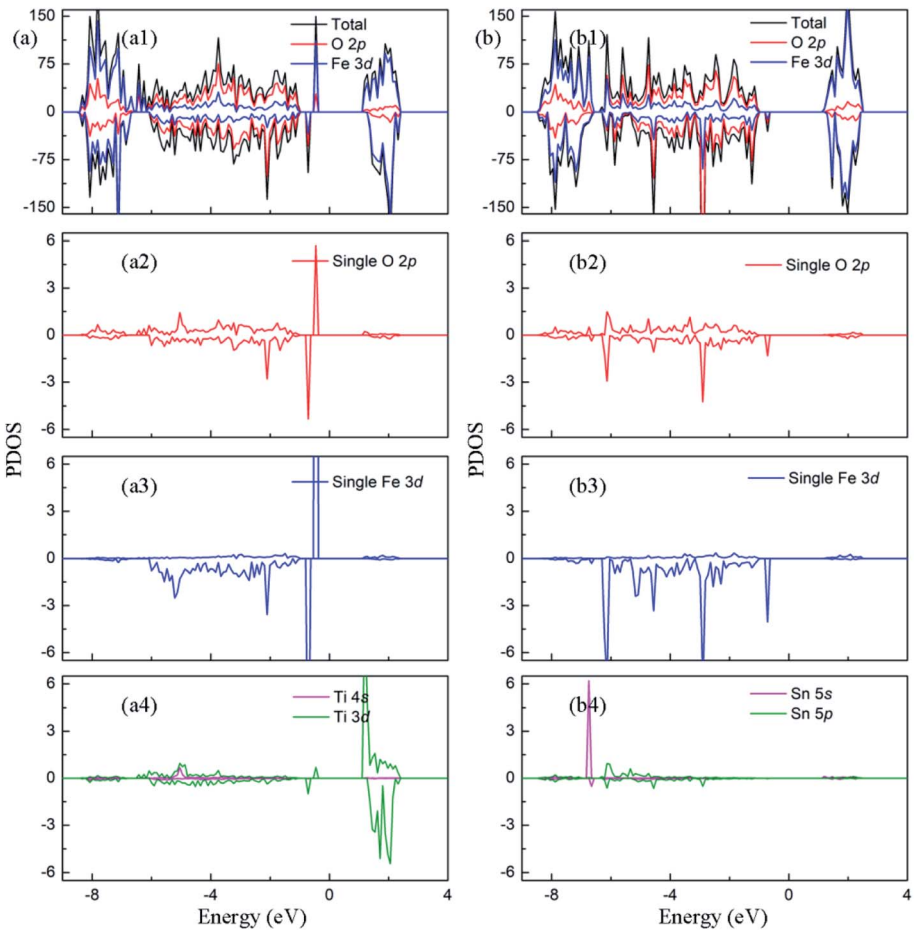


Fig. 5 The projected density of states of (a) $(Ti_{Fe} + V_O)$–$Fe_2O_3$ (b) $(Sn_{Fe} + V_O)$–$Fe_2O_3$. The Fermi level is set to zero.

minimum in the system with doped Sn ions and oxygen vacancy. As shown in Fig. 5(b2) and (b3), Fe 3d have obvious hybridization with O 2p in the range of −1–−6 eV, and the occupied energy level is introduced into the bandgap. The magnetic moment of Fe atom changes to 3.63 $\mu_B$ due to the change of electron configuration in 3d orbital. In ($Sn_{Fe}$ + $V_O$)–$Fe_2O_3$, the average increase of Fe–O bond length is about 0.018 Å for the five coordinated Fe atom. By comparing the change of bond length, we conclude that the additional nonlocal electrons brought by Sn can also weaken the bonding strength between the Fe and O atoms around the O vacancy, causing the increase of the unbonded electrons in Fe atoms. Therefore, the properties of the donor states possess the electronic properties of Fe 3d and O 2p. The Bader charge analysis indicates that the Fe atom adjacent to O vacancy has 0.5e more than that in $Fe_2O_3$, which leads to local donor levels as mentioned above. The partial charge density plotted in Fig. S3† mainly distribute on the atoms around O vacancy. The co-existence of oxygen vacancy and Sn doping also reduce the bandgap width of hematite to 2.09 eV. From the analysis of electronic properties, synergistic effects of oxygen vacancy and doping make the band gap width decrease, and donor levels appear, which are beneficial to the absorption of photons and the increase of carrier concentration observed in experiment.

The prediction of optical properties helps us to understand optical photons interacting with the electrons in the pure and impurity-contained hematite. The absorption coefficient $\alpha(\omega)$ can be derived from the real and imaginary parts of the dielectric function as follow:

$$\alpha(\omega) = \sqrt{2}\omega\left[\sqrt{\varepsilon_1{}^2(\omega) + \varepsilon_2{}^2(\omega)} - \varepsilon_1(\omega)\right]^{1/2}$$

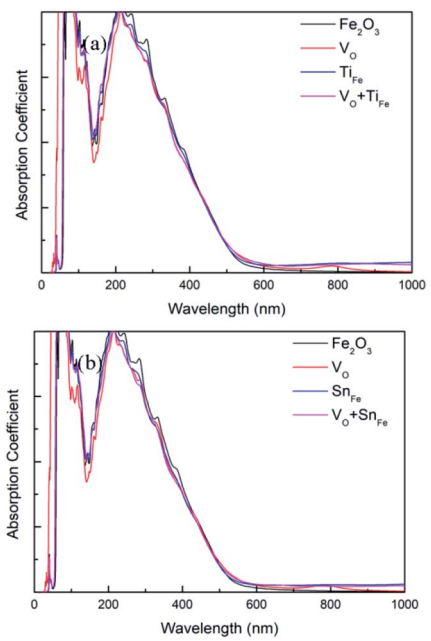


Fig. 6 The absorption coefficient of (a) ($Ti_{Fe}$ + $V_O$)–$Fe_2O_3$ (b) ($Sn_{Fe}$ + $V_O$)–$Fe_2O_3$.

As is shown in Fig. 6, the absorption edge of perfect $Fe_2O_3$ in the visible light region is about 560 nm, which is in agreement with experimental measurements. The optical absorption edge is about 600 nm (or 590 nm) for $Fe_2O_3$ containing O vacancy and Ti atom (or Sn), which is attributed to the bandgap reduction. Besides, it can be seen that low-energy photons (<bandgap) can still be absorbed for the two investigated systems. The reason for the improvement of light absorption ability lies in the deep donor levels, which act as 'steps' in electronic transition from valence band to conduction band. For ($Ti_{Fe}$ + $V_O$)–$Fe_2O_3$ system, the wavelength of the absorbed photons can reach 3600 nm, which corresponds to excite electrons in the valence band to the donor energy level. For the case of ($Sn_{Fe}$ + $V_O$)–$Fe_2O_3$, this value is 3650 nm.

## Conclusions

In brief, this paper investigates the formation mechanisms and the electronic structures of $Fe_2O_3$ with doped atom and oxygen vacancy by first principles calculation. Our results demonstrate that: (1) the oxygen vacancy is easier to be created due to the introduction of doped atom Ti or Sn. (2) The interaction of oxygen vacancy and doping has obvious effects on the electronic structure around the bandgap of hematite. The oxygen vacancy and doped Ti make the bandgap decrease from 2.20 eV to 2.07 eV. Meanwhile, two donor levels are generated at 1.47 eV and 1.73 eV under the bottom of the conduction band, respectively. For the system with oxygen vacancy and doped Sn ions, the bandgap width shrinks to 2.09 eV, and the donor level is introduced at 1.75 eV from the conduction band minimum. (3) The interaction of doping and oxygen vacancy can enlarge visible light absorption edge and improve utilization of low energy photons due to intermediate bands within bandgap.

## Conflicts of interest

There are no conflicts to declare.

## Notes and references

1 A. Fujishima and K. Honda, *Nature*, 1972, **238**, 37.
2 T. Bak, J. Nowotny, M. Rekas and C. C. Sorrell, *Int. J. Hydrogen Energy*, 2002, **27**, 991–1002.
3 P. Merchant, R. Collins, R. Kershaw, K. Dwight and A. Wold, *J. Solid State Chem.*, 1979, **27**, 307–315.
4 A. Kay, I. Cesar and M. Grätzel, *J. Am. Chem. Soc.*, 2006, **128**, 15714–15721.
5 A. B. Murphy, P. R. F. Barnes, L. K. Randeniya, I. C. Plumb, I. E. Grey, M. D. Horne and J. A. Glasscock, *Int. J. Hydrogen Energy*, 2006, **31**, 1999.
6 H. J. Ahn, M. J. Kwak, J. S. Lee, K. Y. Yoon and J. H. Jang, *J. Mater. Chem. A*, 2014, **2**, 19999–20003.
7 N. J. Cherepy, D. B. Liston, J. A. Lovejoy, H. M. Deng and J. Z. Zhang, *J. Phys. Chem. B*, 1998, **102**, 770.
8 Y. Zhang, S. Jiang, W. Song, P. Zhou, H. Ji, W. Ma, W. Hao, C. Chen and J. Zhao, *Energy Environ. Sci.*, 2015, **8**, 1231–1236.

 

9 S. Song, J. Kim, D. Lee, J. Lee, T. Min, J. A. Chae, J. S. Bae, J. Lee, J. S. Lee and S. Park, *J. Am. Ceram. Soc.*, 2017, **100**, 3928–3934.
10 X. Meng, G. Qin, W. A. Goddard III, S. Li, H. Pan, X. Wen, Y. Qin and L. Zuo, *J. Phys. Chem. C*, 2013, **117**, 3779–3784.
11 K. Sivula, R. Zboril, F. Le Formal, R. Robert, A. Weidenkaff, J. Tucek, J. Frydrych and M. Grätzel, *J. Am. Chem. Soc.*, 2010, **132**, 7436.
12 G. Wang, Y. Ling, H. Wang, L. Xihong and Y. Li, *J. Photochem. Photobiol. C Photochem. Rev.*, 2014, **19**, 35.
13 Y. Ling, G. Wang, D. A. Wheeler, J. Z. Zhang and Y. Li, *Nano Lett.*, 2011, **11**, 2119–2125.
14 M. N. Huda, A. Walsh, Y. Yan, S. H. Wei and M. M. Al-Jassim, *J. Appl. Phys.*, 2010, **107**, 123712.
15 J. A. Glasscock, P. R. F. Barnes, I. C. Plumb and N. Savvides, *J. Phys. Chem. C*, 2007, **111**, 44.
16 M. Zhang, W. Luo, Z. Li, T. Yu and Z. Zou, *Appl. Phys. Lett.*, 2010, **97**, 042105.
17 J. Deng, J. Zhong, A. Pu, D. Zhang, M. Li, X. Sun and S. T. Lee, *J. Appl. Phys.*, 2012, **112**, 084312.
18 Y. Ling, G. Wang, J. Reddy, C. Wang, J. Z. Zhang and Y. Li, *Angew. Chem., Int. Ed.*, 2012, **51**, 4074–4079.
19 M. Li, J. Deng, A. Pu, P. Zhang, H. Zhang, J. Gao, Y. Hao, J. Zhong and X. Sun, *J. Mater. Chem. A*, 2014, **2**, 6727–6733.
20 M. Rioult, D. Stanescu, E. Fonda, A. Barbier and H. Magnan, *J. Phys. Chem. C*, 2016, **120**, 7482–7490.
21 T. Y. Yang, H. Y. Kang, U. Sim, Y. J. Lee, J. H. Lee, B. Koo, K. T. Nam and Y. C. Joo, *Phys. Chem. Chem. Phys.*, 2013, **15**, 2117–2124.
22 A. Pu, J. Deng, M. Li, J. Gao, H. Zhang, Y. Hao, J. Zhong and X. Sun, *J. Mater. Chem. A*, 2014, **2**, 2491–2497.
23 Z. Wang, X. Mao, P. Chen, M. Xiao, S. Monny, S. Wang, M. Konarova, A. Du and L. Wang, *Angew. Chem.*, 2019, **131**(4), 1042–1046.
24 Y. Zhou, M. Yan, J. Hou, Y. Niu, D. Ni, H. Shen, P. Niu and Y. Ma, *Sol. Energy*, 2019, **179**, 99–105.
25 Z. Zhou, S. Wu, L. Qin, L. Li, L. Li and X. Li, *J. Mater. Chem. A*, 2018, **6**, 15593–15602.
26 J. Wang, N. H. Perry, L. Guo, L. Vayssieres and H. L. Tuller, *ACS Appl. Mater. Interfaces*, 2018, **11**(2), 2031–2041.
27 G. Kresse and J. Furthmüller, *Phys. Rev. B: Condens. Matter Mater. Phys.*, 1996, **54**, 11169.
28 G. Kresse and D. Joubert, *Phys. Rev. B: Condens. Matter Mater. Phys.*, 1999, **59**, 1758.
29 J. Perdew, K. Burke and M. Ernzerhof, *Phys. Rev. Lett.*, 1996, **77**, 3865.
30 H. J. Monkhorst and J. D. Pack, *Phys. Rev. B: Condens. Matter Mater. Phys.*, 1976, **13**, 5188.
31 S. L. Dudarev, G. A. Botton, S. Y. Savrasov, C. J. Humphreys and A. P. Sutton, *Phys. Rev. B: Condens. Matter Mater. Phys.*, 1998, **57**, 1505.
32 N. J. Mosey, P. Liao and E. A. Carter, *J. Chem. Phys.*, 2008, **129**, 014103.
33 M. Tang, J. X. Shang and Y. Zhang, *RSC Adv.*, 2018, **8**, 640.
34 L. W. Finger and R. M. Hazen, *J. Appl. Phys.*, 1980, **51**, 5362.
35 Y. Sato and S.-I. Akimoto, *J. Appl. Phys.*, 1979, **50**, 5285.
36 P. Kumar, P. Sharma, R. Shrivastav, S. Dass and V. R. Satsangi, *Int. J. Hydrogen Energy*, 2011, **36**, 2777.
37 J. H. Seo, K. Choi, J. Nam, H. Lee and J. H. Lee, *Appl. Catal., B*, 2020, **260**, 118186.